ACS OMEGA

Open Access

http://pubs.acs.org/journal/acsodf

Article

Provenance Analysis in the Nima Basin during Paleogene and Its Implications for the Decline of the Tibetan Central Valley

Yuhang Luo, Wentian Mi,* Yuan Gao, and Luqing Qin

Cite This: *ACS Omega* 2024, 9, 13148−13162

Read Online

ACCESS | Metrics & More | Article Recommendations

ABSTRACT: It is unclear what caused the Bangong Nujiang suture zone in the central Tibetan plateau to rise from less than 2 km in early Cenozoic to more than 4 km at present. The zircon U−Pb ages and trace elements of samples from the Niubao Formation in the Paleogene of the Nima basin were analyzed and tested. Combined with the isostasy theory, the surface uplift height of the Nima Basin during the Cenozoic period was calculated. The zircon U−Pb age results of the Niubao formation are consistent with the ages of the Lhasa terrane on the south side of the basin, the Qiangtang terrane on the north side, and the uplift in central. The zircon Eu/Eu* results show that the crust in central part of Tibetan plateau thickened by ∼20 km in Paleogene, resulting in ∼3 km surface uplift. Sediments created a total of about 1 km of surface uplift throughout the Paleogene, and the deposition rate began to slow down significantly at ∼40 Ma. Therefore, it is inferred that in the early Cenozoic, the uplift of the valley was mainly caused by sedimentation. With the continuous downward subduction of the Indian plate, at about 40 Ma, factors such as crustal shortening dominated the uplift of the central valley, and the uplift caused by deposition only accounted for a very small part. In general, the uplift of the Central Valley in the Paleogene was mainly affected by crustal shortening, but a quarter of the surface uplift was caused by the accumulation of sediments.

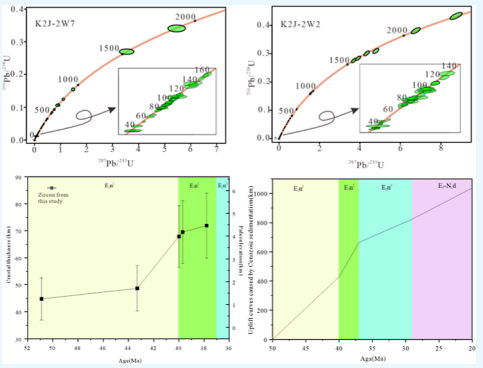

1. INTRODUCTION

Tibetan plateau is the highest plateau in the world at present. Its uplift directly affects the global climate, environment, and biological evolution.[1−3] It has always been a hot area of geoscience research. However, the process of plateau uplift, especially the uplift of the central plateau, is still controversial. The Proto-Tibetan Plateau model suggests that the central Tibet formed by the Lhasa terrane and the Qiangtang terrane uplifted to the present height in the late Cretaceous and then gradually expanded to both sides.[4−6] However, some recent studies suggest that the central Tibetan plateau may have been the topography of a high undulating valley before the plateau formed.[7,8]

Currently, Bangong Nujiang suture zone in central Tibet is elevated to a height of over 4 km.[9] The discovery of foraminiferal fossils shows that the Eocene elevation of the Gaize basin in the western part of Bangong Nujiang suture zone is equal to the sea level.[10] The response of the late Oligocene cyclic strata to the monsoon in the Daze Co area of the Nima basin in the middle of the suture also indicates that the area is still at a relatively low altitude at 25 Ma.[11] The discovery of fish fossils and leaf fossils in the Lunpola basin of the eastern part of the suture,[12,13] as well as the results of palynological studies in this area,[14,15] all indicate that prior to 25 Ma ago, the elevation of the Lunpola basin remained relatively low. During the same period, significantly higher than 4 km is the elevation of the Qiangtang terrane on the northern side of the basin and the Lhasa terrane on the southern side, resulting in a geomorphological pattern of two mountains flanking a valley.[7]

However, currently, the central part of the plateau exhibits a low-relief plateau landscape. The mechanism through which this region evolved from a valley to its present geomorphology has not been conclusively determined. The subduction of Indian plate to Eurasian plate leads to the crustal thickening and asthenosphere upwelling in the central part of Tibet, which may jointly cause the demise of the central valley.[7,16] Nevertheless, some scholars believe that the internal flow basins formed in the early Cenozoic are the key to the low undulating landforms.[17] Nevertheless, there is no clear constraint on which factor is the main factor of uplift, and there is no clear model to accurately explain the uplift mode of the central plateau.

During the valley's demise, a sequence of sedimentary basins were created, namely, Lunpola, Nima, and Gaize basins, arranged in an east−west direction.[16] These basins record the

Received: December 5, 2023
Revised: February 3, 2024
Accepted: February 14, 2024
Published: March 6, 2024

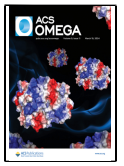

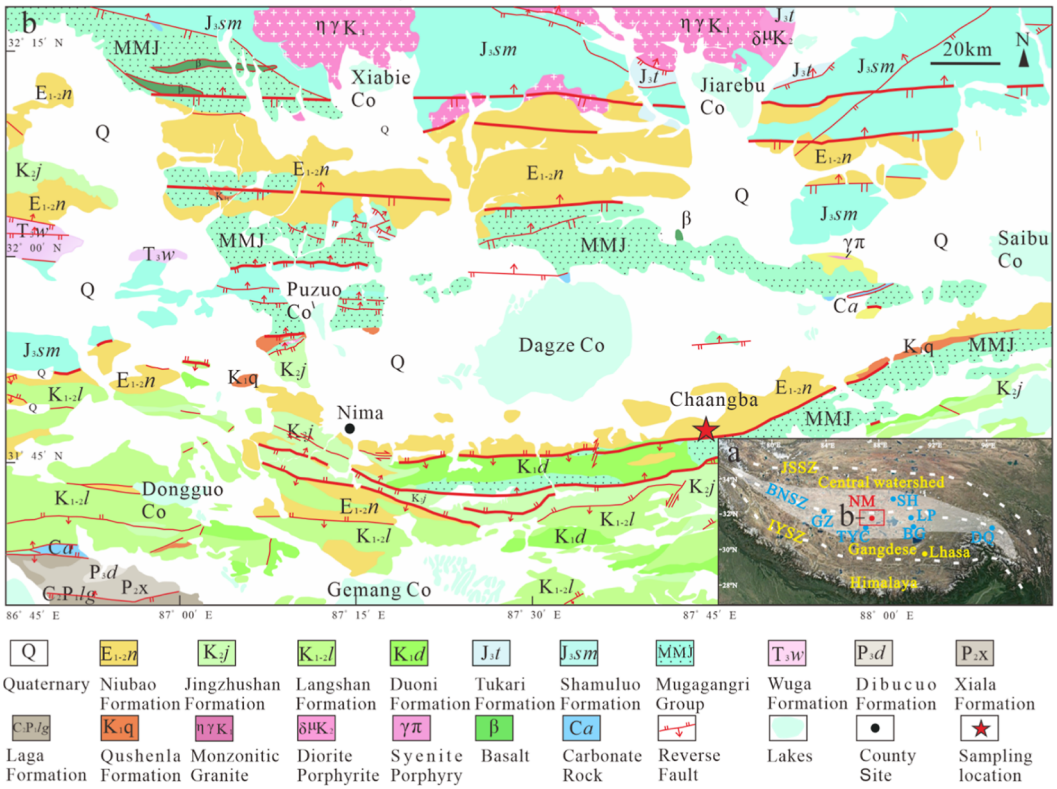

Figure 1. (a) Topography of the Tibetan plateau and neighboring regions illustrating the main tectonic boundaries, the extent of the Central Tibetan valley (white shaded area), the location of the Nima basin (red dots), and other Cenozoic basins (blue dots). BG, Bangor basin; DQ, Dingqing basin; GZ, Gerze basin; LP, Lunpola basin; NM, Nima basin; SH, Shuanghu basin; TYC; Tangra Yum Co basin; IYSZ, Indus-Yarlung suture zone; JSSZ, Jinsha suture zone; BNST, Bangong-Nujiang suture zone. Adapted with permission from ref 7. Copyright 2022 Science. (b) Geological map of Nima basin. Adapted with permission from ref 22. Copyright 2022 China University of Geosciences, Beijing.

paleoclimate, paleogeography, and tectonic setting of the time.[18−20] Nima basin is a good research object because of its thick Paleogene deposits (Figure 1).[21] Previous studies on this basin have mostly focused on the sedimentary evolution process of the basin itself with less research on the driving mechanisms and geodynamic processes behind it.

This study conducted zircon U−Pb dating on Paleogene sediments of the Nima Basin, inferring its potential provenance. Combined with the theory of isostasy, the crustal thickness change of the Nima basin during Paleogene was restored using the method of zircon Eu/Eu*, and the surface uplift height caused by the accumulation of Paleogene sediments was calculated by an empirical formula. By comparing the results of field investigations, the reconstruction of the tectonic evolution during Paleogene can provide scientific evidence for the demise of the central valley in Tibet Plateau.

2. GEOLOGICAL SETTING AND LITHOSTRATIGRAPHY

Nima basin is located in the middle part of the Bangong Nujiang suture zone in the central part of Tibetan plateau, adjacent to Lunpola basin to the east and Gaize basin to the west. It is separated from the Lhasa terrane by the Gaize Siling Co fault to the south and from the Qiangtang terrane by the Muggar thrust fault to the north (Figure 1). Due to the multiple tectonic activities of the Bangong Nujiang suture zone, the center uplift split Nima basin into the southern depression and the northern depression.[21] The Paleogene sediments in the Nima Basin are mainly Niubao formation and Dingqinghu formation. Niubao formation is mainly composed of a set of mudstone, shale, carbonate, and sandstone of shallow lacustrine facies. The strata can be divided into three members, from bottom to top, the first member, the second member, and the third member of Niubao formation. The first member of the Niubao formation is a set of purple−red sandstone, locally intercalated with gray−green and purple−red mudstone, which contradicts with the underlying strata of the Mesozoic. The seismic data show that the maximum thickness is 1300 m. The second member of the Niubao formation is a set of gray black mudstone with shale deposits, with oil shale and siltstone locally visible, with a sedimentary thickness of up to 1000 m. The third member of Niubao Formation is mainly composed of grayish−green mudstone and siltstone, with a thickness greater than 1000 m. The Dingqinghu formation is a set of purple−red and gray−green clastic rocks of deep lake facies and fluvial facies, which are parallelly unconformably overlain by the mudstone of the Niubao formation, and partially intercalated with oil shale and marl.[23]

On the basis of clarifying the structural characteristics of the Nima basin, the Chaangba section (31°49′39.32″ and 87°49′34.85″) was selected for research. The lower member of the Chaangba section is the Niubao formation, which is mainly composed of a purple−gray thick conglomerate and purple reddish brown medium sandstone with brown−yellow middle-thick sandstone or conglomerate. The upper member of the section belongs to the Dingqinghu formation. From top to bottom, it gradually transitions from gray shale with gray thin dolomite to purple thick conglomerate with mudstone and sandstone (Figure 2).

https://doi.org/10.1021/acsomega.3c09706
ACS Omega 2024, 9, 13148−13162

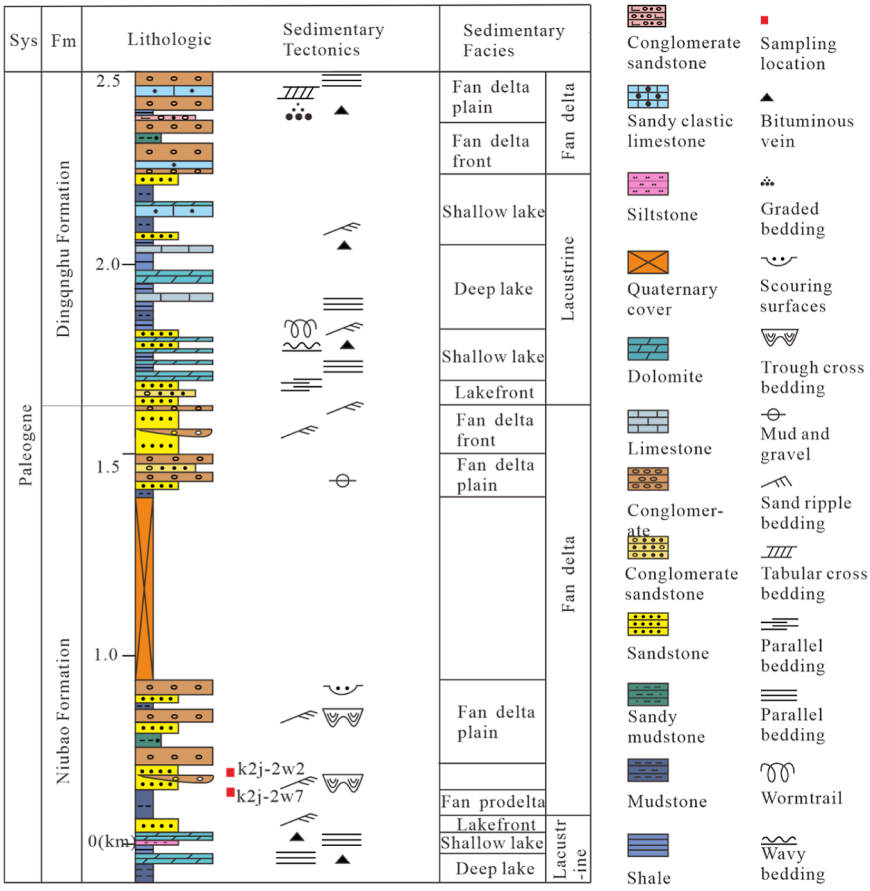

Figure 2. Stratigraphic column of the Chaangba section in the Nima Basin. Adapted with permission from ref 24.

3. METHODS

3.1. Zircon U−Pb. The properties of zircon are very stable, and the U−Pb age of zircon in sedimentary rocks records the time of zircon crystallization. Due to its resistance to changes brought about by weathering, transit, sedimentation, and diagenesis within the basin, it is frequently utilized for sediment source investigation.[25] This analysis method is extremely effective, especially for geological bodies with different crystallization ages at the periphery of the basin.[26,27]

Sandstone samples k2j-2w7 (87°49′34″, 31°49′39″) and k2j-2w2 (87°49′34″, 31°49′39″) were collected from the Chaangba section in the southern depression for experiments.

The sample pretreatment was carried out in Langfang Yuheng Mine Rock Technology Service Co., Ltd., and the target preparation was completed in Xi'an Tuohang Geological Technology Service Co., Ltd. First, the selected fresh samples were crushed to 80−100 mesh, and then, the crushed rock samples are sorted using electromagnetic separation and heavy liquid elutriation methods. Zircon particles are picked out using a binocular mirror. Zircon grains that are large and transparent and have a good crystal structure under a binocular microscope were carefully selected. Then, the zircon grains were neatly adhered onto a double-sided adhesive. Finally, the epoxy resin was poured. After being dried and curing, the target was polished to highlight the zircon. The obtained CL images were examined at Key Laboratory of Mineral resources in Western China (Gansu Province) to examine zircon characteristic. The American Agilent 7700x laser ablation inductively coupled plasma mass spectrometer joint a 193 nm excimer laser ablation system was used for the experiments. He is the carrier gas, the erosion depth is 20 μm, and the laser beam spot diameter is 30 μM. For each analysis of five zircon points, an international standard zircon 91500 is used as the external standard, and the element content calculation is corrected using NIST SRM610. The data was processed using GLITER (4.0) software.[28] U−Pb concordia diagrams for samples and Kernel density estimation (KDE) plots were drawn by IsoplotR software.[29] The $^{206}Pb/^{238}U$ ages were used for young zircons (<1000 Ma), and the $^{207}Pb/^{206}Pb$ ages for earlier zircons (>1000 Ma). The error of individual test data and the error of $^{206}Pb/^{238}U$ age weighted average are both 1σ. The analysis results are listed in Table 1.

3.2. Zircon Eu/Eu*. Garnet is usually enriched with heavy rare earth elements, and Y and Yb are preferentially separated into garnet under high-pressure conditions. The high Sr/Y and La/Yb ratios of neutral calc-alkaline rocks indicate that garnet appears as a residual phase in the source. Both the subducted eclogitic oceanic crust and the thickened eclogitic lower crust can produce intermediate magma with high La/Yb and Sr/Y ratios. The La/Yb and Sr/Y ratios of the intermediate arc magma essentially reflect the mineral assemblage (garnet + plagioclase + amphibole) of the source. The trace element ratios (such as La/Yb and Sr/Y) of the samples can be used to indicate crustal thickness.[30] Although this method has been successfully applied,[31] its samples require extensive sampling in a large area of the field, and the availability of the samples is relatively limited. Zircon Eu/Eu* is positively correlated with La/Yb, and it is relatively easy to obtain the data. Therefore, the thickness of crustal uplift can be calculated by zircon Eu/Eu*.[32] The acquisition of zircon trace element data is the same as that of 3.1,

https://doi.org/10.1021/acsomega.3c09706
ACS Omega 2024, 9, 13148−13162

Table 1. LA-ICP-MS U−Pb Isotopic Results of Detrital Zircons from the Nima Basin

measuring point no	$w(B)/10^{-6}$			isotope ratio and error						age (Ma) and error					
	Th	U	Th/U	$^{207}Pb/^{206}Pb$	1σ	$^{207}Pb/^{235}U$	1σ	$^{206}Pb/^{238}U$	1σ	$^{207}Pb/^{206}Pb$	1σ	$^{207}Pb/^{235}U$	1σ	$^{206}Pb/^{238}U$	1σ
							K2j-2w7								
k2j-2w7-1	312.41	263.36	1.19	0.05071	0.00225	0.09198	0.00423	0.01392	0.0002	228	80	89	4	89	1
k2j-2w7-2	56.9	485.95	0.12	0.07545	0.00085	1.4844	0.02474	0.15424	0.00194	1081	16	924	10	925	11
k2j-2w7-3	71.78	193.45	0.37	0.05122	0.00097	0.08867	0.0018	0.01348	0.00017	251	25	86	2	86	1
k2j-2w7-4	97.16	254.65	0.38	0.08493	0.0008	2.00948	0.02452	0.18908	0.00235	1314	11	1119	8	1116	13
k2j-2w7-5	765.42	684.54	1.12	0.05069	0.00057	0.12254	0.00157	0.0186	0.00023	227	13	117	1	119	1
k2j-2w7-6	387.67	518.38	0.75	0.04906	0.00068	0.08815	0.00135	0.0134	0.00017	151	16	86	1	86	1
k2j-2w7-7	50.38	277.77	0.18	0.05484	0.00061	0.3642	0.00486	0.05012	0.00062	406	13	315	4	315	4
k2j-2w7-8	345.88	260.39	1.33	0.05368	0.0011	0.10656	0.00232	0.01595	0.0002	358	27	103	2	102	1
k2j-2w7-9	197.74	407	0.49	0.11889	0.00139	5.4619	0.13793	0.3408	0.00434	1940	27	1895	22	1891	21
k2j-2w7-10	114.55	112.8	1.02	0.054	0.00485	0.04682	0.00422	0.00771	0.00014	371	171	46	4	49.5	0.9
k2j-2w7-11	128.73	301.48	0.43	0.05911	0.00093	0.44498	0.00871	0.05972	0.00076	571	22	374	6	374	5
k2j-2w7-12	263.94	249.15	1.06	0.04965	0.00128	0.24455	0.0072	0.03491	0.00046	179	44	222	6	221	3
k2j-2w7-13	344.3	632.86	0.54	0.04841	0.00075	0.11981	0.00205	0.01788	0.00022	119	19	115	2	114	1
k2j-2w7-14	83.98	169.56	0.50	0.05382	0.00169	0.15176	0.00517	0.02237	0.00031	364	52	143	5	143	2
k2j-2w7-16	292.19	464.12	0.63	0.04809	0.02183	0.07497	0.03423	0.01167	0.0006	104	694	73	32	75	4
k2j-2w7-17	153.49	199.52	0.77	0.05312	0.00123	0.11606	0.00286	0.01741	0.00022	334	33	111	3	111	1
k2j-2w7-18	126.85	341.82	0.37	0.0584	0.00073	0.67781	0.0105	0.08488	0.00105	545	16	525	6	525	6
k2j-2w7-19	296.06	265.29	1.12	0.04931	0.00124	0.09303	0.00248	0.01406	0.00018	163	39	90	2	90	1
k2j-2w7-20	1148.21	503.75	2.28	0.04854	0.00081	0.08627	0.00156	0.01326	0.00016	126	22	84	1	85	1
k2j-2w7-21	172.79	71.45	2.42	0.05767	0.00088	0.75822	0.01577	0.0928	0.00116	517	25	573	9	572	7
k2j-2w7-22	309.86	410.98	0.75	0.04798	0.00061	0.28855	0.00442	0.04079	0.0005	98	17	257	3	258	3
k2j-2w7-23	518.7	666.27	0.78	0.05308	0.00164	0.10163	0.00335	0.0152	0.00021	332	50	98	3	97	1
k2j-2w7-24	853.12	1352.3	0.63	0.048	0.00081	0.09943	0.00185	0.01511	0.00019	99	22	96	2	97	1
k2j-2w7-25	133.95	132.3	1.01	0.05184	0.00165	0.10128	0.00335	0.01516	0.0002	278	51	98	3	97	1
k2j-2w7-26	1194.89	1527.04	0.78	0.04729	0.00059	0.11112	0.0016	0.01672	0.0002	64	15	107	1	107	1
k2j-2w7-27	519.02	444.48	1.17	0.05114	0.00077	0.17397	0.00303	0.02548	0.00032	247	19	163	3	162	2
k2j-2w7-28	1468.69	1581.34	0.93	0.03598	0.00239	0.11729	0.0081	0.01768	0.00024	−34	226	113	7	113	2
k2j-2w7-29	4662.78	2623.02	1.78	0.05306	0.00232	0.07001	0.00314	0.01087	0.00015	331	77	69	3	69.7	1
k2j-2w7-30	432.02	683.1	0.63	0.04977	0.0006	0.16986	0.00242	0.02507	0.00031	184	15	159	2	160	2
k2j-2w7-31	377.24	394.5	0.96	0.04869	0.00071	0.19361	0.00331	0.02821	0.00035	133	19	180	3	179	2
k2j-2w7-32	114.95	146.44	0.78	0.04134	0.00198	0.09201	0.00453	0.01394	0.00018	−214	89	89	4	89	1
k2j-2w7-33	268.65	196.31	1.37	0.04653	0.00148	0.07552	0.00249	0.01147	0.00015	25	47	74	2	73.5	1
k2j-2w7-34	728.04	581.93	1.25	0.04429	0.00103	0.10859	0.0027	0.01641	0.0002	−56	32	105	2	105	1
k2j-2w7-35	76.59	57.51	1.33	0.06988	0.00087	2.22436	0.04675	0.20244	0.00247	925	24	1189	15	1188	13
k2j-2w7-36	141.81	263.5	0.54	0.04753	0.00089	0.10669	0.0022	0.016	0.0002	76	26	103	2	102	1
k2j-2w7-37	426.04	484.01	0.88	0.04731	0.00063	0.1628	0.00252	0.02405	0.00029	65	17	153	2	153	2
k2j-2w7-38	103.15	131.35	0.79	0.06104	0.00073	1.10736	0.01847	0.12448	0.00151	641	17	757	9	756	9
k2j-2w7-39	256.64	461.37	0.56	0.05892	0.00062	0.91595	0.01228	0.1079	0.0013	564	13	660	7	661	8
k2j-2w7-40	95.31	91	1.05	0.04105	0.00634	0.03808	0.00589	0.00586	0.00009	−230	222	38	6	37.7	0.6
k2j-2w7-41	118.96	155.94	0.76	0.04422	0.00071	0.27511	0.00538	0.03895	0.00047	−59	23	247	4	246	3
k2j-2w7-42	122.21	267.37	0.46	0.04316	0.00099	0.09375	0.00231	0.01421	0.00018	−115	34	91	2	91	1

https://doi.org/10.1021/acsomega.3c09706
ACS Omega 2024, 9, 13148−13162

Table 1. continued

measuring point no	$w(B)/10^{-6}$			isotope ratio and error						age (Ma) and error					
	Th	U	Th/U	$^{207}Pb/^{206}Pb$	1σ	$^{207}Pb/^{235}U$	1σ	$^{206}Pb/^{238}U$	1σ	$^{207}Pb/^{206}Pb$	1σ	$^{207}Pb/^{235}U$	1σ	$^{206}Pb/^{238}U$	1σ
K2j-2w7															
k2j-2w7-43	112.11	218.02	0.51	0.0478	0.00161	0.14433	0.00522	0.0214	0.00028	89	59	137	5	136	2
k2j-2w7-44	149.02	184.08	0.81	0.05108	0.0009	0.10335	0.00205	0.01563	0.00019	244	24	100	2	100	1
k2j-2w7-45	247.9	386.79	0.64	0.05162	0.00059	0.49015	0.00704	0.06492	0.00078	269	15	405	5	405	5
k2j-2w7-46	185.98	354.67	0.52	0.04442	0.00083	0.11086	0.00232	0.01668	0.00021	−49	24	107	2	107	1
k2j-2w7-47	143.1	440.25	0.33	0.0577	0.00089	0.49262	0.00973	0.06483	0.00079	518	23	407	7	405	5
k2j-2w7-48	151.05	175.77	0.86	0.04443	0.00109	0.09708	0.00256	0.0148	0.00018	−48	34	94	2	95	1
k2j-2w7-49	122.79	122.04	1.01	0.04429	0.00092	0.11537	0.00272	0.01735	0.00022	−56	29	111	2	111	1
k2j-2w7-50	155.18	161.21	0.96	0.05079	0.00164	0.09851	0.00333	0.01493	0.00019	231	54	95	3	96	1
k2j-2w7-51	325.13	978.35	0.33	0.04417	0.00056	0.11702	0.00178	0.01758	0.00021	−62	16	112	2	112	1
k2j-2w7-52	231.67	225.33	1.03	0.0469	0.00122	0.10427	0.00288	0.01566	0.00019	44	40	101	3	100	1
k2j-2w7-53	527.19	537.74	0.98	0.04485	0.00074	0.11146	0.00208	0.01675	0.0002	−27	18	107	2	107	1
k2j-2w7-54	601.69	1025.36	0.59	0.04428	0.0007	0.05929	0.00106	0.00918	0.00011	−56	20	58	1	58.9	0.7
k2j-2w7-55	1141.23	561.97	2.03	0.04326	0.00071	0.10114	0.00189	0.01522	0.00018	−109	22	98	2	97	1
k2j-2w7-56	195.59	121.71	1.61	0.06347	0.00171	0.89365	0.03308	0.10598	0.00137	724	56	648	18	649	8
k2j-2w7-58	264.06	464.79	0.57	0.0416	0.00129	0.14244	0.00483	0.02237	0.00029	−199	54	135	4	143	2
k2j-2w7-59	345.51	310.8	1.11	0.05226	0.00098	0.14877	0.00317	0.0219	0.00027	297	27	141	3	140	2
k2j-2w7-60	181.4	195.15	0.93	0.05468	0.00108	0.32727	0.00776	0.04571	0.00056	399	32	287	6	288	3
k2j-2w7-61	153.75	147.55	1.04	0.04652	0.00116	0.11203	0.00306	0.01685	0.00021	25	37	108	3	108	1
k2j-2w7-62	64.3	463.37	0.14	0.10577	0.00127	6.54299	0.16746	0.37538	0.00449	1728	30	2052	23	2055	21
k2j-2w7-63	249.31	226.11	1.10	0.04291	0.00123	0.10583	0.00324	0.01601	0.0002	−128	46	102	3	102	1
k2j-2w7-64	55.59	124.98	0.44	0.03752	0.00097	0.08446	0.00239	0.01304	0.00016	−439	171	82	2	84	1
k2j-2w7-65	429.35	721.92	0.59	0.04251	0.00141	0.12096	0.00431	0.01815	0.00023	−149	58	116	4	116	1
k2j-2w7-66	301.4	257.93	1.17	0.03734	0.00207	0.0394	0.00222	0.00613	0.00008	−450	249	39	2	39.4	0.5
k2j-2w7-67	213.51	426.92	0.50	0.04256	0.00071	0.12378	0.00239	0.01862	0.00022	−147	24	118	2	119	1
k2j-2w7-68	166.9	308.16	0.54	0.18081	0.00194	19.47201	0.37182	0.60777	0.00713	2660	17	3066	18	3061	29
k2j-2w7-69	271.01	132.35	2.05	0.0572	0.00828	0.04086	0.00592	0.00618	0.00014	499	285	41	6	39.7	0.9
k2j-2w7-70	148.24	165.17	0.90	0.09585	0.00157	3.54297	0.11471	0.26973	0.00335	1545	42	1537	26	1539	17
K2j-2w2															
k2j-2w2-1	182.17	196.27	1.08	0.0488	0.00123	0.10944	0.00289	0.01651	0.00019	138	40	105	3	106	1
k2j-2w2-2	585.26	540.93	0.92	0.04895	0.00108	0.04843	0.00111	0.00749	0.00009	145	32	48	1	48.1	0.6
k2j-2w2-3	71.38	254.96	3.57	0.04692	0.00088	0.30248	0.00624	0.04255	0.00048	45	28	268	5	269	3
k2j-2w2-4	331.46	345.44	1.04	0.04794	0.00103	0.10255	0.00235	0.01486	0.00017	96	33	99	2	95	1
k2j-2w2-5	287.51	250.91	0.87	0.09922	0.00105	3.90084	0.05649	0.28342	0.0032	1610	12	1614	12	1609	16
k2j-2w2-6	68.18	102.76	1.51	0.05591	0.00252	0.11095	0.00513	0.01596	0.0002	449	81	107	5	102	1
k2j-2w2-7	87.66	138.87	1.58	0.04958	0.00183	0.08615	0.00329	0.0134	0.00017	175	65	84	3	86	1
k2j-2w2-8	173.02	204.09	1.18	0.05268	0.00308	0.04163	0.00245	0.00622	0.00008	315	111	41	2	40	0.5
k2j-2w2-9	134.13	203.31	1.52	0.13492	0.00139	6.75585	0.09102	0.38122	0.00431	2163	11	2080	12	2082	20
k2j-2w2-10	537.93	414.53	0.77	0.09765	0.001	3.68756	0.04544	0.2756	0.00312	1580	10	1569	10	1569	16
k2j-2w2-11	141.75	154.73	1.09	0.05058	0.00183	0.10943	0.00408	0.0163	0.00019	222	65	105	4	104	1
k2j-2w2-12	893.23	578.91	0.65	0.04804	0.00265	0.04154	0.00231	0.00622	0.00008	101	100	41	2	40	0.5
k2j-2w2-13	82.19	114.33	1.39	0.04627	0.00159	0.09424	0.00337	0.01413	0.00017	12	53	91	3	90	1

https://doi.org/10.1021/acsomega.3c09706
ACS Omega 2024, 9, 13148−13162

Table 1. continued

measuring point no	$w(B)/10^{-6}$			isotope ratio and error						age (Ma) and error					
	Th	U	Th/U	$^{207}Pb/^{206}Pb$	1σ	$^{207}Pb/^{235}U$	1σ	$^{206}Pb/^{238}U$	1σ	$^{207}Pb/^{206}Pb$	1σ	$^{207}Pb/^{235}U$	1σ	$^{206}Pb/^{238}U$	1σ
							K2j-2w2								
k2j-2w2-14	417.69	791.08	1.89	0.05544	0.00059	0.42772	0.00532	0.05785	0.00066	430	12	362	4	363	4
k2j-2w2-15	270.59	282.72	1.04	0.04502	0.00231	0.04701	0.00245	0.00792	0.00011	−18	84	47	2	50.9	0.7
k2j-2w2-16	268.84	289.53	1.08	0.04724	0.00144	0.05226	0.00164	0.00792	0.00009	61	50	52	2	50.9	0.6
k2j-2w2-17	260.23	242.14	0.93	0.05237	0.00103	0.12191	0.00257	0.01798	0.00021	302	27	117	2	115	1
k2j-2w2-18	174.7	364.66	2.09	0.07266	0.00075	1.56097	0.01971	0.1598	0.00182	1004	11	955	8	956	10
k2j-2w2-19	382.08	378.95	0.99	0.05037	0.00144	0.11198	0.00335	0.01657	0.0002	212	47	108	3	106	1
k2j-2w2-20	261.6	558.59	2.14	0.04902	0.00056	0.27982	0.00374	0.03929	0.00045	149	14	251	3	248	3
k2j-2w2-21	103.48	69.2	0.67	0.0391	0.0057	0.04456	0.00653	0.00674	0.00011	−343	232	44	6	43.3	0.7
k2j-2w2-22	263.98	271.79	1.03	0.04018	0.00214	0.03702	0.00199	0.00588	0.00007	−279	105	37	2	37.8	0.4
k2j-2w2-23	396.67	686.2	1.73	0.05083	0.00059	0.24238	0.00325	0.03503	0.0004	233	14	220	3	222	2
k2j-2w2-24	89.47	125.3	1.40	0.04956	0.00146	0.13806	0.00427	0.02056	0.00025	174	49	131	4	131	2
k2j-2w2-25	917.9	478.65	0.52	0.04713	0.00173	0.04316	0.00161	0.00603	0.00007	56	61	43	2	38.8	0.4
k2j-2w2-26	409.61	620.79	1.52	0.04664	0.00066	0.10616	0.00167	0.01699	0.0002	31	18	102	2	109	1
k2j-2w2-27	107.9	143.23	1.33	0.05136	0.00144	0.10125	0.00299	0.01589	0.0002	257	45	98	3	102	1
k2j-2w2-28	674.36	929.53	1.38	0.05056	0.00078	0.05922	0.00099	0.00838	0.0001	221	19	58.4	0.9	53.8	0.6
k2j-2w2-29	265.01	316.34	1.19	0.04857	0.00087	0.12186	0.00236	0.01808	0.00021	127	25	117	2	116	1
k2j-2w2-30	221.88	415.93	1.87	0.05161	0.00093	0.09412	0.00184	0.01289	0.00015	268	24	91	2	82.6	1
k2j-2w2-31	174.64	499.61	2.86	0.05403	0.00062	0.3767	0.00513	0.05055	0.00059	372	14	325	4	318	4
k2j-2w2-32	123.89	242.74	1.96	0.04832	0.00109	0.08953	0.00213	0.01328	0.00016	115	34	87	2	85	1
k2j-2w2-33	169.39	536.98	3.17	0.10668	0.00106	4.78713	0.06051	0.30957	0.00357	1743	10	1783	11	1739	18
k2j-2w2-34	81.86	460.79	5.63	0.11134	0.00111	5.08539	0.06692	0.28834	0.00333	1821	11	1834	11	1633	17
k2j-2w2-35	103.61	174.97	1.69	0.05104	0.00206	0.10165	0.00422	0.01421	0.00018	243	72	98	4	91	1
k2j-2w2-36	847.51	2104.14	2.48	0.05018	0.00135	0.20016	0.00482	0.02893	0.00035	203	64	185	4	184	2
k2j-2w2-37	66.44	144.13	2.17	0.05006	0.00255	0.08707	0.0045	0.01372	0.00017	198	97	85	4	88	1
k2j-2w2-38	154.52	236.51	1.53	0.04887	0.00229	0.10985	0.00497	0.0163	0.0002	141	107	106	5	104	1
k2j-2w2-39	78.66	146.84	1.87	0.05108	0.00182	0.09103	0.00336	0.01312	0.00017	244	61	88	3	84	1
k2j-2w2-40	78.46	194.64	2.48	0.04353	0.00149	0.07851	0.00276	0.01236	0.00015	−95	56	77	3	79.2	1
k2j-2w2-41	114.51	232.12	2.03	0.04589	0.00112	0.08718	0.00225	0.01319	0.00016	−8	30	85	2	84	1
k2j-2w2-42	72.86	419.31	5.76	0.05543	0.00061	0.54595	0.00747	0.0713	0.00083	430	14	442	5	444	5
k2j-2w2-43	30.55	26.58	0.87	0.20657	0.00214	10.06169	0.21258	0.4614	0.00546	2879	19	2440	20	2446	24
k2j-2w2-44	192.35	201.34	1.05	0.04852	0.00115	0.08871	0.00223	0.01317	0.00016	125	37	86	2	84	1
k2j-2w2-45	168.71	252.81	1.50	0.04422	0.00086	0.12203	0.00258	0.01799	0.00022	−59	26	117	2	115	1
k2j-2w2-46	98.77	174.51	1.77	0.04844	0.00155	0.09112	0.00302	0.01395	0.00017	121	55	89	3	89	1
k2j-2w2-47	124.21	397.62	3.20	0.10307	0.00101	4.3345	0.05557	0.30113	0.00352	1680	11	1700	11	1697	17
k2j-2w2-48	194.27	343.15	1.77	0.04645	0.00091	0.07581	0.00158	0.01181	0.00014	21	27	74	1	75.7	0.9
k2j-2w2-49	775.57	941.16	1.21	0.05249	0.00077	0.0545	0.00087	0.00727	0.00009	307	17	53.9	0.8	46.7	0.6
k2j-2w2-50	354.57	705.33	1.99	0.06025	0.0006	0.87338	0.01068	0.10397	0.00122	613	12	637	6	638	7
k2j-2w2-51	236.07	427.05	1.81	0.05726	0.00061	0.4732	0.00617	0.06383	0.00075	502	13	393	4	399	5
k2j-2w2-52	163.53	406.69	2.49	0.14149	0.00138	8.74946	0.12341	0.43315	0.0051	2246	11	2312	13	2320	23
k2j-2w2-53	257.28	316.49	1.23	0.04578	0.00078	0.09347	0.00173	0.0144	0.00017	−14	18	91	2	92	1
k2j-2w2-54	98.69	294.86	2.99	0.04772	0.00091	0.08045	0.00165	0.01225	0.00015	85	26	79	2	78.5	1

https://doi.org/10.1021/acsomega.3c09706
ACS Omega 2024, 9, 13148−13162

Table 1. continued

measuring point no	w(B)/10^{-6}			isotope ratio and error						age (Ma) and error					
	Th	U	Th/U	$^{207}Pb/^{206}Pb$	1σ	$^{207}Pb/^{235}U$	1σ	$^{206}Pb/^{238}U$	1σ	$^{207}Pb/^{206}Pb$	1σ	$^{207}Pb/^{235}U$	1σ	$^{206}Pb/^{238}U$	1σ
							K2j-2w2								
k2j-2w2-55	92.72	137.85	1.49	0.04426	0.00131	0.09014	0.00277	0.01406	0.00017	−57	43	88	3	90	1
k2j-2w2-56	242.76	192.77	0.79	0.05385	0.00102	0.11073	0.00229	0.01584	0.00019	365	26	107	2	101	1
k2j-2w2-57	96.57	190.65	1.97	0.04538	0.00115	0.08181	0.00219	0.01265	0.00016		32	80	2	81	1
k2j-2w2-58	127.08	314.66	2.48	0.04986	0.00088	0.13434	0.00264	0.01952	0.00024	188	24	128	2	125	2
k2j-2w2-59	1336.06	2706.05	2.03	0.05328	0.00335	0.04283	0.00263	0.00583	0.00008	341	146	43	3	37.5	0.5
k2j-2w2-60	358.25	314.17	0.88	0.04615	0.00124	0.04751	0.00132	0.00719	0.00009	5	35	47	1	46.2	0.6

which is obtained at the same time as the zircon U−Pb experiment.

3.3. Thickness of Sediments. For the internal flow basin, there are two reasons for the surface uplift of the basin. One is the shortening of the crust, and another is the accumulation of sediments. When the basin's basement is relatively rigid and crustal shortening is limited, sedimentation may play a leading role in the uplift of the passively constrained basin.[33] By observing the thickness of sediments in the basin, the height of surface uplift caused by sediments can be calculated by isostasy theory (Figure 3).[34] The thickness data of the sediments used to calculate the crustal thickness of the central Tibetan are from the Ni 1 well and Zangshuangdi 1 well. Combined with the surface outcrops with good exposure, the mean value is taken.

4. RESULTS

4.1. Zircon U−Pb Data. In terms of the morphological characteristics of zircon, the ratio of length to width of some zircon particles is larger, subangular, and columnar. Others have a small ratio of length to width, semiself-shaped, and rounded, indicating that they have been transported over long distances. The zircon grains are 50−150 μm in size and show brown or rose color under transmitted light. The CL image of zircon has obvious rhythmic zoning (Figures 4 and 5), and the Th/U ratio of zircon is mostly greater than 0.4, which can be identified as magmatic crystallization zircon.[35]

Sample k2j-2w2 obtained 57 effective zircon U−Pb dating spots (concordance degree of the measured points is between 90 and 110%) (Figure 4 and Table 1), with ages ranging from 83 to 2246 Ma. These ages were mainly distributed into the following ranges: 37.8−53.8 Ma, 75.7−99 Ma, 101−131 Ma, 184−269 Ma, 318−444 Ma, 638−956 Ma, 1580−1743 Ma, 2163 Ma, 2246 Ma. After analyzing the 70 points of the sample k2j-2w7, 64 effective zircon U−Pb dating spots were obtained that met the concordance degree (90−110%) (Figure 5 and Table 1). The age values varied between 37 and 1728 Ma. It mainly includes the following intervals: 37.7−58.9, 69.7−97, 100−119, 136−179, 221−405, 525−925, 1545, and 1728 Ma.

4.2. Zircon Eu/Eu* Data. Crustal thickness can be reconstructed using europium anomalies in zircon (Eu/Eu*, which means chondrite normalized $Eu/\sqrt{Sm \times Gd}$).[32,36] The empirical formula for calculating crustal thickness from zircon Eu/Eu* is as follows: $H = (84.2 \pm 9.2) \times Eu/Eu^{*}zircon + (24.5 \pm 3.3)$. Zircon data with Th/U < 0.1 and La > 1 ppm were deleted,[32,36] and five meaningful values obtained to calculate crustal thickness. Based on Airy isostasy, the height of surface uplift caused by crustal thickening can be calculated from the formula.[37] The findings indicate that the crustal thickness of Nima basin increased by ∼20 km during the Paleogene and caused a surface uplift of ∼3 km (Figure 6 and Table 2).

4.3. Uplift Caused by the Paleogene Sedimentation. Based on the Airy isostasy theory, the condition of isostatic compensation can be expressed as[34]

$$\int_0^{h_b} \rho_b(h)\,\mathrm{d}h = \int_{h_b}^{H_B} [\rho_m - \rho_b(h)]\,\mathrm{d}h \quad (1)$$

Formula 2 can be derived from formula 1, which is the calculation formula for the uplift amplitude (h_b) caused by sedimentation

$$h_b = \frac{\rho_m - \rho_0}{\rho_m} H_B - \frac{\rho_0 - \rho_S}{c\rho_m}(e^{-cH_B} - 1) \quad (2)$$

https://doi.org/10.1021/acsomega.3c09706
ACS Omega 2024, 9, 13148−13162

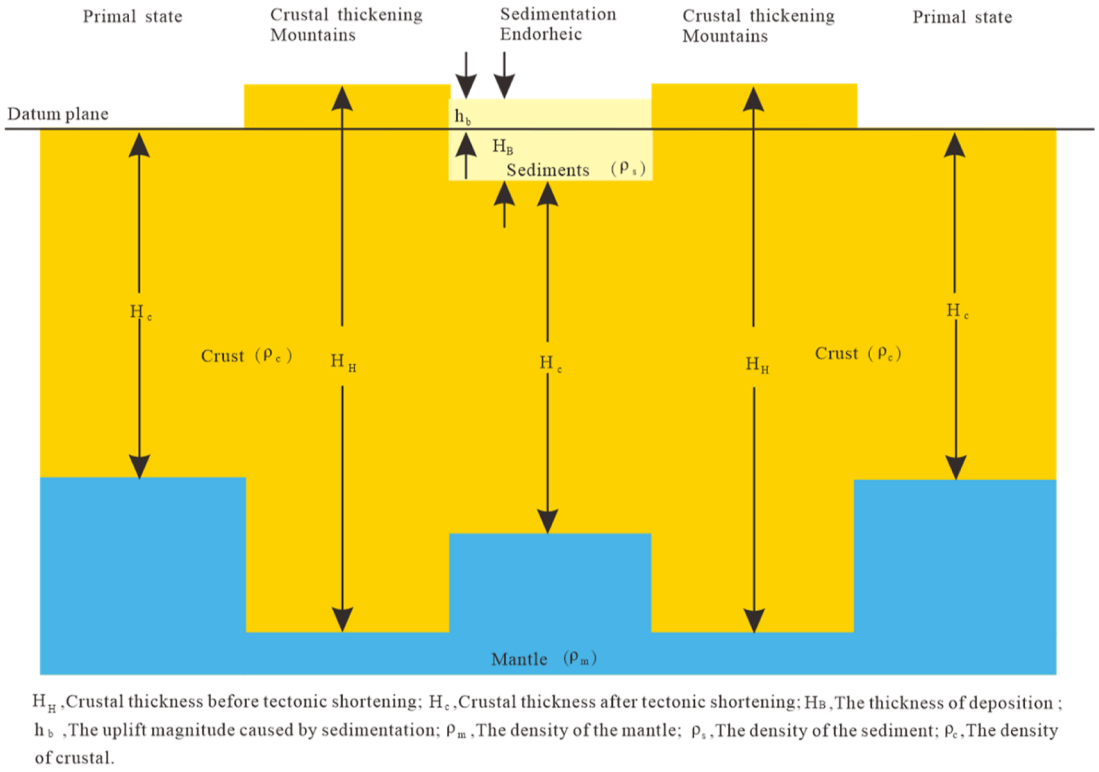

Figure 3. Schematic diagram of surface uplift caused by the accumulation of sediments. Adapted with permission from ref 34. Copyright 2021 Pergamon-Elsevier Science Ltd.

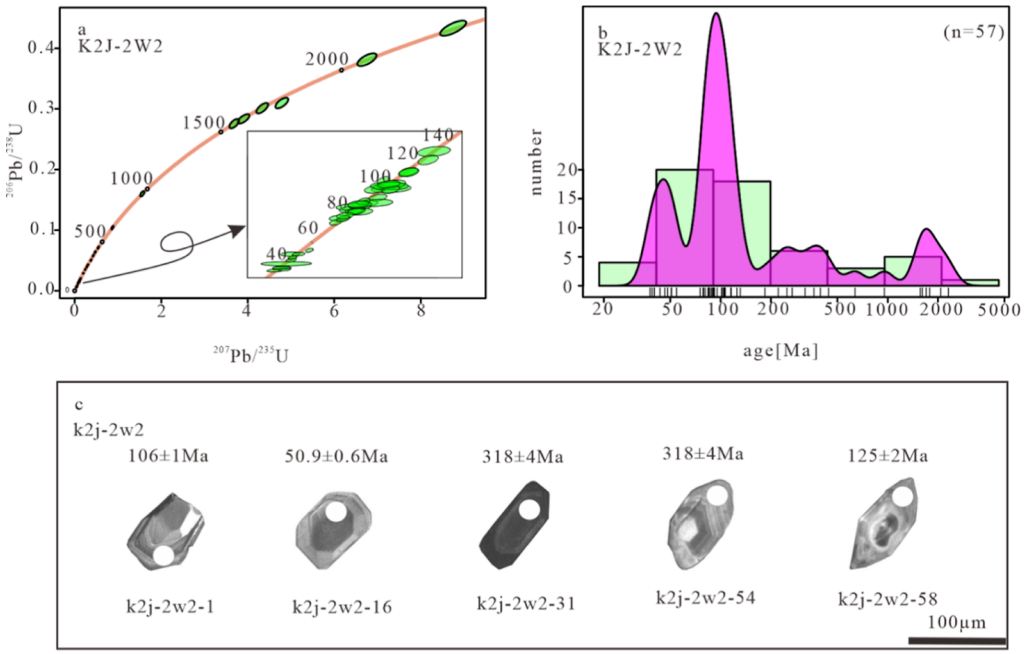

Figure 4. U−Pb concordia diagrams (a) and KDE plots (b) for k2j-2w2. Cathodoluminescence images of representative zircon grains (c) from samples of k2j-2w2. In each frame, the top number is the U−Pb age, and the bottom number is the point number of zircon.

H_B is the thickness of deposition. ρ_m is the density of the mantle and adopted as 3.3×10^3 kg/m^3. ρ_0 is the grain density and adopted as 2.7×10^3 kg/m^3. ρ_s is the density of surface sediments and adopted as 2.2×10^3 kg/m^3. c is a constant and adopted 4×10^{-4} m^{-1}.

The deeper the sediment, the greater its compaction degree; therefore, it is necessary to correct the sediment thickness (H_P) in the estimation of paleoelevation.

$$\int_0^{H_P} \rho_b(h)\,dh = \int_{H_B - H_M}^{H_B} \rho_b(h)\,dh \tag{3}$$

Formula 4 can be derived from formula 3

https://doi.org/10.1021/acsomega.3c09706
ACS Omega 2024, 9, 13148−13162

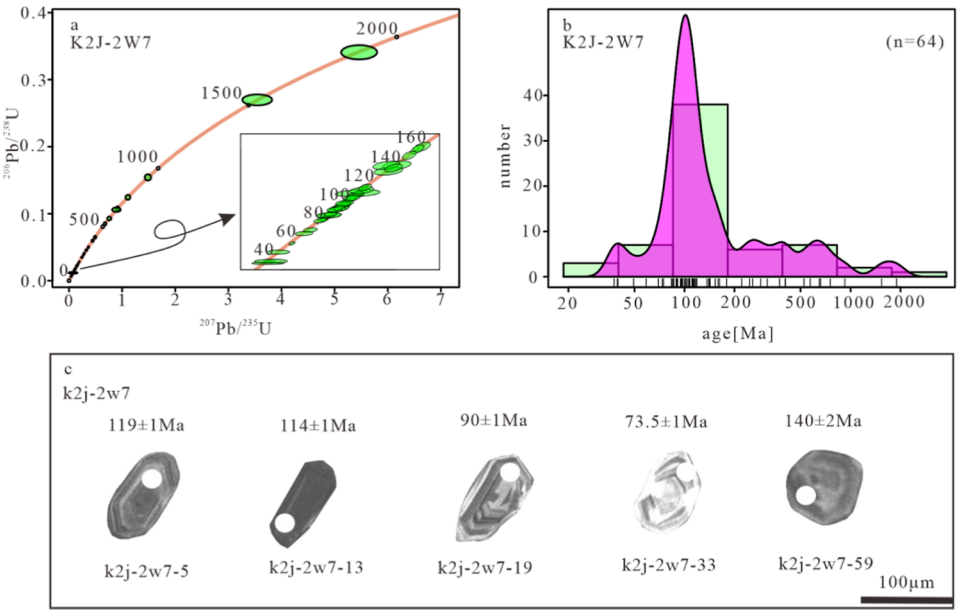

Figure 5. U−Pb concordia diagrams (a) and KDE plots (b) for k2j-2w7. Cathodoluminescence images of representative zircon grains (c) from samples of k2j-2w7. In each frame, the top number is the U−Pb age, and the below number is the point number of zircon.

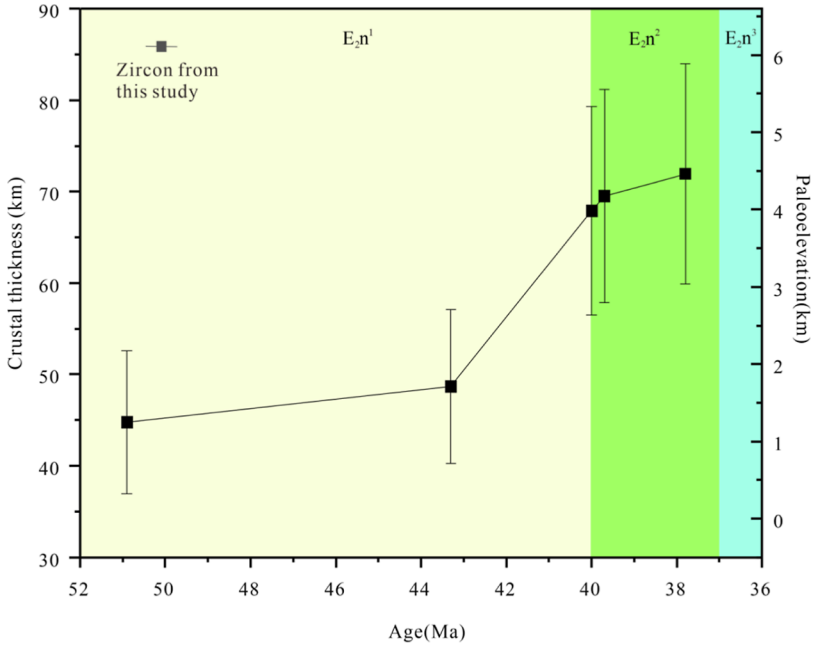

Figure 6. Crustal thickness and paleoelevation evolution of the Nima basin reconstructed from the Cenozoic zircon Eu/Eu* (N = 5).

Table 2. Reconstructing Crustal Thickness Evolution from Europium Anomalies in Zircons

analysis	La (ppm)	Sm (ppm)	Eu (ppm)	Gd (ppm)	Th (ppm)	U (ppm)	Th/U	Eu/Eu*	crustal thickness (km)	paleoelevation (km)
k2j-2w2-22	0.0848	4.19	1.628	18.62	263.98	271.79	0.971264579	0.56325493	71.92606507	4.615758134
k2j-2w7-69	0.434	17.59	5.11	48.53	271.01	132.35	2.047676615	0.534478556	69.50309441	4.312886801
k2j-2w2-12	0.0412	5.25	1.754	20.61	893.23	578.91	1.542951409	0.515297923	67.88808512	4.11101064
k2j-2w2-21	0.1015	12.34	2.034	37.97	103.48	69.2	1.495375723	0.287157736	48.67868138	1.709835172
k2j-2w2-16	0.567	4.24	0.783	23.3	268.84	289.53	0.928539357	0.240740037	44.77031116	1.221288895

$$\rho_0 H_P + \frac{1}{c}(\rho_0 - \rho_s)(e^{-cH_P} - 1) = \rho_0 H_M + \frac{1}{c}(\rho_0 - \rho_s)(e^{-cH_B} - e^{-c(H_B - H_M)}) \quad (4)$$

The corrected deposition thickness (H_P) can be calculated by formula 4.

According to the above formula, the surface uplift caused by the sediment in Nima basin during Paleogene is calculated to be

https://doi.org/10.1021/acsomega.3c09706
ACS Omega 2024, 9, 13148−13162

~1 km. At about 37 Ma, the deposition rate of the basin was significantly slowed down (Figure 7 and Table 3).

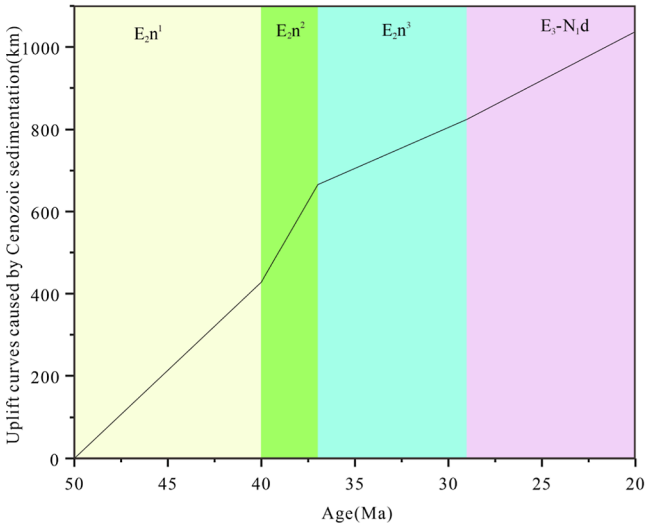

Figure 7. Uplift curves caused by Cenozoic sedimentation.

Table 3. Uplift Magnitude Caused by Cenozoic Sedimentation of the Lunpola Basin[a]

periods	age (Ma)	thickness (m)	H_M (m)	H_P (m)	h_b (m)
beginning of Cenozoic	>50	0	0	0	0
the first member of Niubao formation	40	1300	1300	1440	428
the second member of Niubao formation	37	930	2230	2380	665
the third member of Niubao formation	29	710	2940	3060	824
Dingqing Lake formation	20	1100	4040	4040	1038

[a]Age, the age of each formation at the end of deposition;[7] thickness, the average thickness of each formation measured in different areas;[38−40] H_M, the thickness of the strata studied in modern observations; H_P, after the calculation of formula 4, the corrected formation thickness; h_b, surface uplift induced by the accumulation of sediments calculated from formula 2.

5. DISCUSSION

5.1. Provenance Analysis of the Nima Basin. The detrital zircon ages of Paleogene sediments in the Nima basin exhibit distinct stages. k2j-2w7 sample (37.7−58.9, 69.7−97 Ma) and k2j-2w2 sample (37.8−53.8, 75.7−99 Ma) can correspond to the ages of the Paleogene volcanic rock in Linzizong group (66−50, 52−47, 53−42 Ma).[41,42] The group is widely distributed in the Lhasa terrane, and the comparable detrital zircon ages suggest that the Lhasa terrane may be a provenance of the Nima basin.

The peak age of detrital zircons in the study region is 110 Ma in the range of 100−130 Ma, which can correspond the Puzuoco granite age (~110 Ma) in the central uplift of Nima basin[6] and Daze granite (105−100 Ma) in the southern margin.[43] This indicates that the basin may have received provenance from magmatic rocks within the suture zone. Jurassic−Cretaceous magmatic activities in the Lhasa terrane are developed, especially the multistage magmatic activities in the late Cretaceous, which formed the granites with high Sr and low Y similar to adakites.[19,44−50] The magmatic rocks developed in this period may correspond to the ages of k2j-2w7 samples (69.7−97, 100−119, and 136−179 Ma) and k2j-2w2 samples (75.7−99, 101−131, and 184−269 Ma). This suggests that the Jurassic−Cretaceous multistage magmatic activity of the Lhasa terrane may provide provenance for the Nima basin. The widely developed arc magmatism at 180−150 Ma in the southern Qiangtang terrane[51] resulted in the formation of basalts and granite porphyry (~110 Ma)[52] in the Gaize area and the Xiabiecuo granite (118 Ma)[6] in the northern margin of the Nima Basin. These ages are consistent with the age of the k2j-2w7 sample (100−119 Ma) and the k2j-2w2 sample (101−131 Ma). This indicates that the peak age of ~110 Ma detrital zircons in the Paleogene of the Nima basin can be compared with the peak age of igneous rocks in potential provenance areas such as the Qiangtang terrane and Lhasa terrane. These Early Cretaceous igneous rocks may be the provenance of the Paleogene in the Nima basin (Figure 8).

The peak value of detrital zircons in Qiangtang terrane and Lhasa terrane is mostly concentrated in Precambrian.[53−59] These peaks correspond to the ages of k2j-2w7 samples (525−925, 1545, and 1728 Ma) and k2j-2w2 samples (638−956, 1580−1743, 2163, and 2246 Ma). It can be seen that the Nima basin samples have age characteristics of detrital zircons from the Lhasa terrane and the Qiangtang terrane.

Overall, the Lhasa terrane, the Qiangtang terrane, and the central uplift of the basin are all potential source areas of the Nima basin.

5.2. Denudation Process of Provenance in the Nima Basin. The reactivation of the pre-existing structural zone in the Bangong Nujiang suture zone formed the Nima basin.[16] In the early Cretaceous, the Nima basin was a single broad basin. Due to the subduction of the Indian plate to the Eurasian plate, the Nima basin was continuously squeezed in space. The Puxu Co fault in the middle of the Nima basin began to be active at ~110 Ma, and the central uplift zone of the basin gradually formed. The early single broad basin was divided into three parts: southern depression, northern depression, and central uplift, and this landform has been maintained until modern times (Figures 9 and 10). The age of detrital zircons shows that the Lhasa terrane on the south side of the basin, the Qiangtang terrane on the north side, and the central uplift in the middle provide provenance for Cenozoic sediments. However, according to the paleogeography and geomorphology of the Nima basin, the provenance of the southern depression is mainly from the Lhasa terrane and the central uplift, and the provenance of the northern depression is mainly from the Qiangtang terrane and the central uplift. Combined with the results of geothermochronology, after the formation of a geomorphological pattern of two depressions and uplifts in the Nima basin, the internal drainage system gradually developed. The tectonic activity of 70−30 Ma made the source areas such as the central uplift zone continuously denuded[17] and transported to the bottom of the basin through the developed internal drainage system and finally deposited huge thick red sediments.

5.3. Form of the Demise of the Central Valley. The downward subduction of the Indian plate activated the pre-existing structural zone of the Bangong Nujiang suture zone and controlled the formation of the Cenozoic basin in the central plateau. During the early Cenozoic, the tectonic belt in the central plateau was constantly active and the internal water system gradually formed. The provenance of the denudation area was transported by the internal water system, and slow lacustrine deposition began at the bottom of the basin. At this

https://doi.org/10.1021/acsomega.3c09706
ACS Omega 2024, 9, 13148−13162

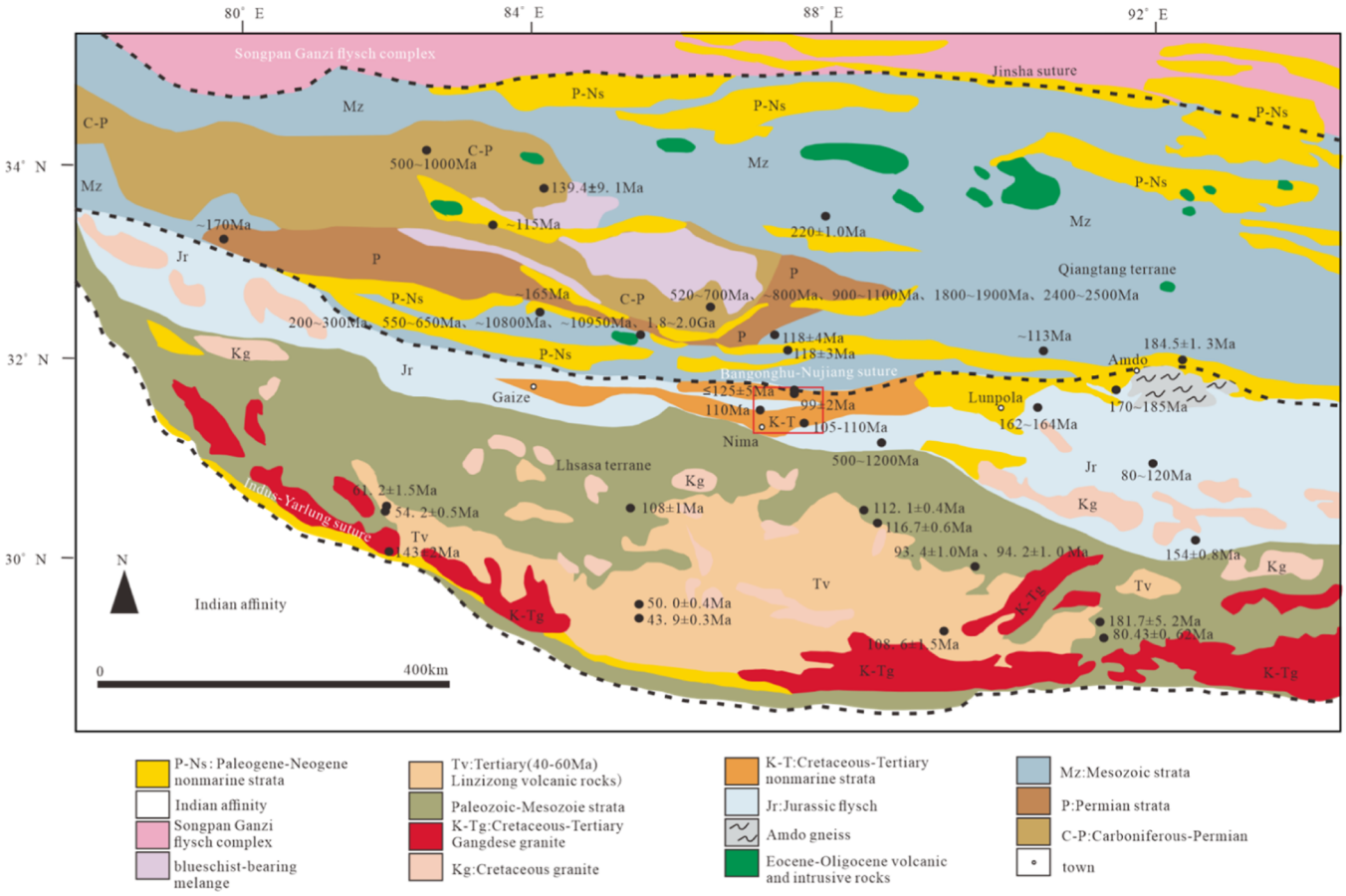

Figure 8. Tectonic map of southern and central Tibet. The black dots represent the region and time of magmatic activity in southern and central Tibet, and the red boxes represent the location of the study region. Adapted with permission from ref 60. Copyright 2005 Geological Society of America.

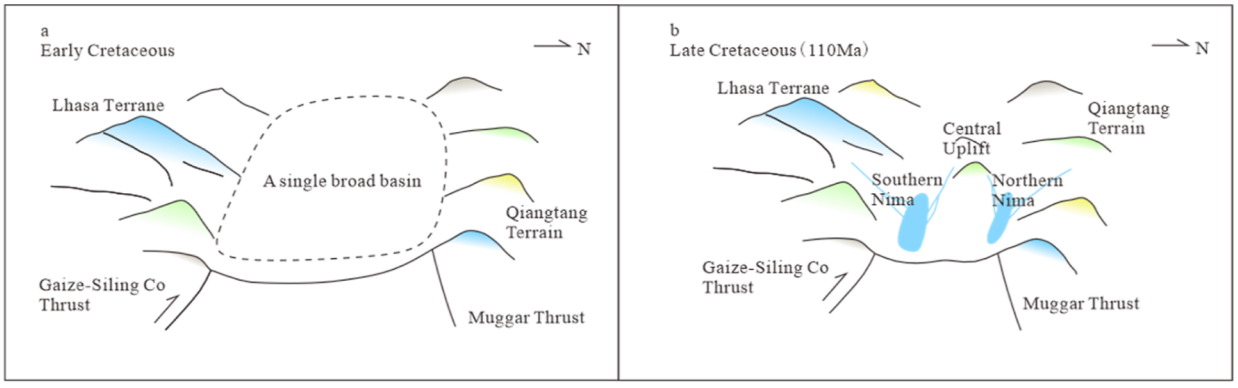

Figure 9. Paleogeographic map of the Nima basin.

time, the uplift of the central valley of the Tibet plateau is mainly caused by the uplift caused by sediment accumulation.[16,17,34] According to the theory of isostasy, the accumulation of sediments in this basin caused a surface uplift of ∼0.7 km. With the continuous extrusion of the Indian plate, the crust of the central Tibetan started to shorten at ∼40 Ma, and the magma at the bottom continued to rise, making the central valley gradually uplift and the altitude higher and higher.[62−68] It can be seen from Eu/Eu* that the crustal thickness in the middle of the Paleogene plateau increased by ∼20 km, which caused the elevation of the central valley to rise by ∼3 km. Due to the tectonic activity caused by the continuous thickening of the crust, the endorheic basin was also destroyed, and the deposition rate began to gradually slow down (Figure 7 and Table 3). The sediment accumulation caused the surface to rise by ∼0.3 km. In general, the uplift of the Central valley in the Paleogene was mainly affected by the shortening of the upper crust, but the uplift caused by sedimentation also accounted for a large factor (Figure 11).

6. CONCLUSIONS

(1) The Paleogene sediments in the Nima basin are from both the Lhasa terrane and the Qiangtang terrane. At the same time, the central uplift in the middle of the basin also provides a part of the source.

https://doi.org/10.1021/acsomega.3c09706
ACS Omega 2024, 9, 13148−13162

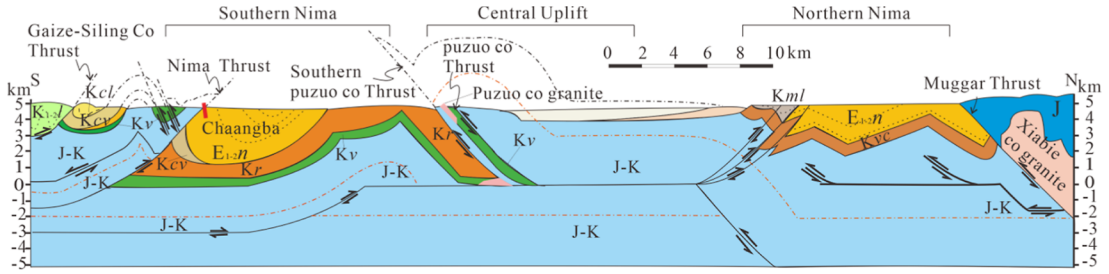

Figure 10. Schematic of the Nima basin cross-sections. J. Jurassic mudstone, shale, siltstone, limestone, turbidite sandstone, metamorphic volcanic rocks; J-K. Jurassic−Cretaceous shale, siltstone, turbidite sandstone, tectonic mélange; $K_{1\text{-}2}$l. Lower Cretaceous Langshan formation limestone; Kvc. Lower Cretaceous volcaniclastic rocks; Kv. Lower Cretaceous volcanic lava, tuff, and volcanic breccia; Kr. Cretaceous red layer; Kcv. Upper Cretaceous volcaniclastic conglomerate; Kcl. Upper Cretaceous carbonate conglomerate; Kml. Upper Cretaceous−Paleocene; Nima basin; $E_{1\text{-}2}$n Paleogene Niubao formation; Chaangba, this measured section. Adapted with permission from ref 61. Copyright 2017 China University of Geosciences, Wuhan.

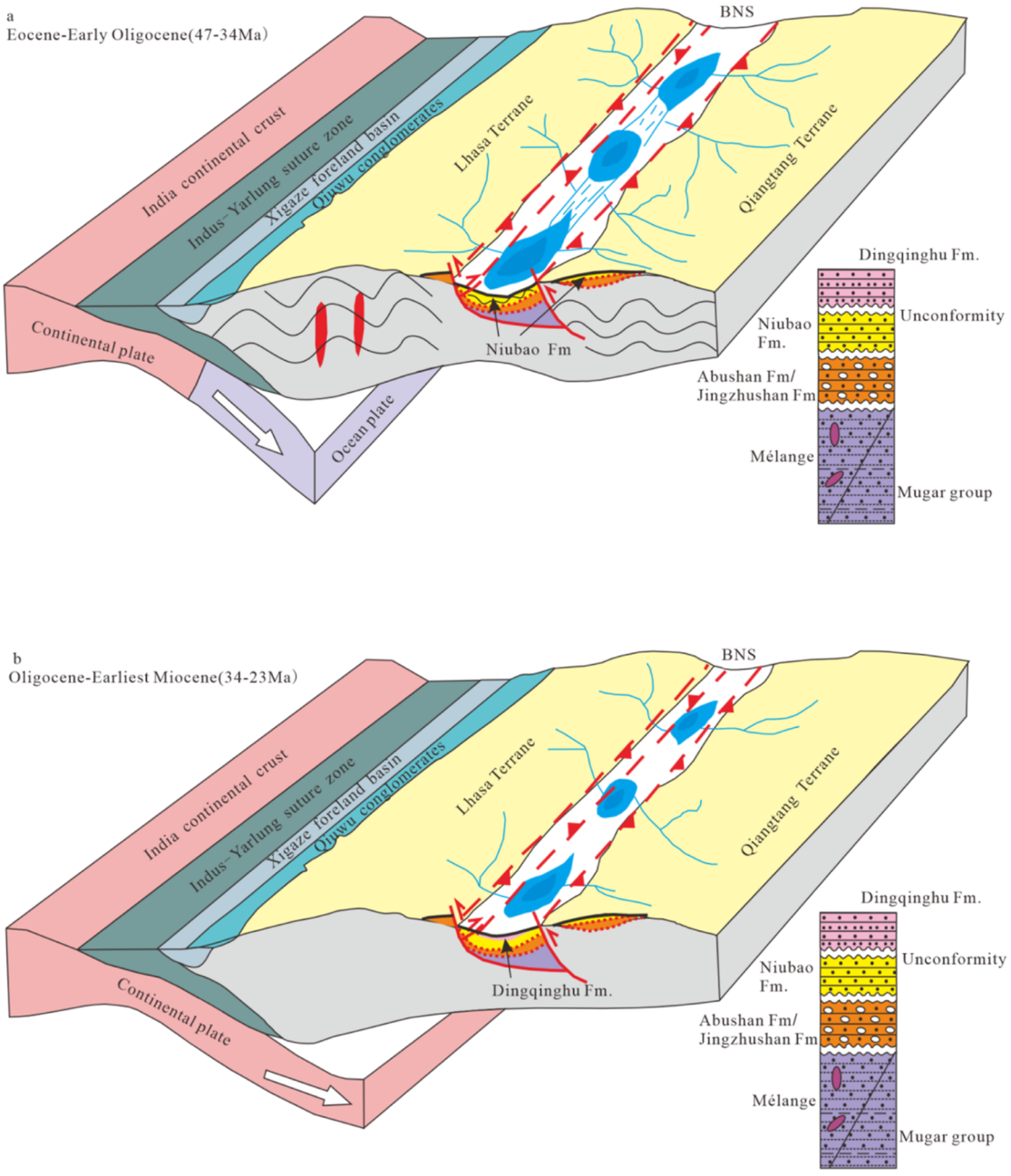

Figure 11. Sketch of the tectonic evolution of the central valley of Tibet during the Paleogene. Adapted with permission from ref 69. Copyright 2022 Elsevier.

https://doi.org/10.1021/acsomega.3c09706
ACS Omega 2024, 9, 13148−13162

(2) During the Paleogene, the Nima basin experienced a total uplift of 4 km, with crustal thickening causing a 3 km uplift and sediment accumulation causing a 1 km uplift.
(3) In the early Cenozoic, the uplift of the valley was mainly caused by sedimentation. With the continuous downward subduction of the Indian plate, the crustal shortening and other factors dominated the uplift of the central valley at ~40 Ma.

AUTHOR INFORMATION

Corresponding Author

Wentian Mi − *School of Resource and Environmental Engineering, Inner Mongolia University of Technology, Hohhot 010051, People's Republic of China*;
Email: miwentian1982@163.com

Authors

Yuhang Luo − *School of Resource and Environmental Engineering, Inner Mongolia University of Technology, Hohhot 010051, People's Republic of China*; orcid.org/0000-0002-8891-0230

Yuan Gao − *School of Resource and Environmental Engineering, Inner Mongolia University of Technology, Hohhot 010051, People's Republic of China*

Luqing Qin − *School of Resource and Environmental Engineering, Inner Mongolia University of Technology, Hohhot 010051, People's Republic of China*

Complete contact information is available at:
https://pubs.acs.org/10.1021/acsomega.3c09706

Notes

The authors declare no competing financial interest.

ACKNOWLEDGMENTS

This work is supported by the National Natural Science Foundation of China (grant no. 42362019) and Inner Mongolia Autonomous Region 2023 Basic Scientific Research Business Project (grant no. ZTY2023063).

REFERENCES

(1) Ao, H.; Dupont-Nivet, G.; Rohling, E. J.; Zhang, P.; Ladant, J.-B.; Roberts, A. P.; Licht, A.; Liu, Q. S.; Liu, Z. H.; Dekkers, M. J.; Coxall, H. K.; Jin, Z. D.; Huang, C. J.; Xiao, G. Q.; Poulsen, C. J.; Barbolini, N.; Meijer, N.; Sun, Q.; Qiang, X. K.; Yao, J.; An, Z. S. Orbital climate variability on the northeastern Tibetan Plateau across theEocene-Oligocene transition. *Nat. Commun.* **2020**, *11* (1), 5249.
(2) Boos, W. R.; Kuang, Z. M. Dominant control of the south Asian monsoon by orographic insulation versus plateau heating. *Nature* **2010**, *463* (7278), 218−222.
(3) Lv, D. W.; Song, Y.; Shi, L. Q.; Wang, Z. L.; Cong, P. Z.; van Loon, A. T. The complex transgression and regression history of the northern margin of the Palaeogene Tarim Sea (NW China), and implications for potential hydrocarbon occurrences. *Mar. Pet. Geol.* **2020**, *112*, 104041.
(4) Zeng, Y. C.; Xu, J. F.; Chen, J. L.; Wang, B. D.; Huang, F. How and how much did western central Tibet raise by India-Asia collision? *Geophys. Res. Lett.* **2022**, *49*, No. e2022GL101206.
(5) Wang, C. S.; Zhao, X. X.; Liu, Z. F.; Lippert, P. C.; Graham, S. A.; Coe, R. S.; Yi, H. S.; Zhu, L. D.; Liu, S.; Li, Y. L. Constraints on the early uplift history of the Tibetan Plateau. *Proc. Natl. Acad. Sci. U.S.A.* **2008**, *105* (13), 4987−4992.
(6) Kapp, P.; DeCelles, P. G.; Gehrels, G. E.; Heizler, M.; Ding, L. Geological records of the Lhasa-Qiangtang and Indo-Asian collisionsin the Nima area of central Tibet. *Geol. Soc. Am. Bull.* **2007**, *119*, 917−933.
(7) Xiong, Z. Y.; Liu, X. H.; Ding, L.; Farnsworth, A.; Spicer, R. A.; Xu, Q.; Valdes, P.; He, S. L.; Zeng, D.; Wang, C.; Li, Z. Y.; Guo, X. D.; Su, T.; Zhao, C. Y.; Wang, H. Q.; Yue, Y. H. The rise and demise of the Paleogene Central Tibetan Valley. *Sci. Adv.* **2022**, *8*, No. eabj0944.
(8) Su, T.; Spicer, R. A.; Wu, F. X.; Farnsworth, A.; Huang, J.; Del Rio, C.; Deng, T.; Ding, L.; Deng, W. Y. D.; Huang, Y. J.; Hughes, A.; Jia, L. B.; Jin, J. H.; Li, S. F.; Liang, S. Q.; Liu, J.; Liu, X. Y.; Sherlock, S.; Spicer, T.; Srivastava, G.; Tang, H.; Valdes, P.; Wang, T. X.; Widdowson, M.; Wu, M. X.; Xing, Y. W.; Xu, C. L.; Yang, J.; Zhang, C.; Zhang, S. T.; Zhang, X. W.; Zhao, F.; Zhou, Z. K. A Middle Eocene lowland humid subtropical "Shangri-La" ecosystem in central Tibet. *Proc. Natl. Acad. Sci. U.S.A.* **2020**, *117*, 32989−32995.
(9) Xie, S. K.; Du, B.; Wang, J.; Peng, Q.; Zhen, B. Characteristics and Distribution Rule of Oil Shale in Lunpola Basin, Tibet. *J. Jilin Univ., Earth Sci. Ed.* **2014**, *44* (6), 1760−1767. (In Chinese with abstract)
(10) Wei, Y.; Zhang, K. X.; Garzione, C. N.; Xu, Y. D.; Song, B. W.; Ji, J. L. Low palaeoelevation of the northern Lhasa terrane during late Eocene: Fossil foraminifera and stable isotope evidence from the Gerze Basin. *Sci. Rep.* **2016**, *6*, 27508.
(11) Jin, C. S.; Xu, D.; Li, M. S.; Hu, P. X.; Jiang, Z. X.; Liu, J. X.; Miao, Y. F.; Wu, F. L.; Liang, W. T.; Zhang, Q.; Su, B.; Liu, Q. S.; Zhang, R.; Sun, J. M. Tectonic and orbital forcing of the South Asian monsoon in central Tibet during the late Oligocene. *Proc. Natl. Acad. Sci. U. S. A.* **2023**, *120* (15), No. e2214558120.
(12) Su, T.; Farnsworth, A.; Spicer, R. A.; Huang, J.; Wu, F. X.; Liu, J.; Li, S. F.; Xing, Y. W.; Huang, Y. J.; Deng, W. Y. D.; Tang, H.; Xu, C. L.; Zhao, F.; Srivastava, G.; Valdes, P. J.; Deng, T.; Zhou, Z. K. No high Tibetan Plateau until the Neogene. *Sci. Adv.* **2019**, *5* (3), No. eaav2189.
(13) Wu, F. X.; Miao, D. S.; Chang, M. M.; Shi, G. L.; Wang, N. Fossil climbing perch and associated plant megafossils indicate a warm and wet central Tibet during the late Oligocene. *Sci. Rep.* **2017**, *7*, 878.
(14) Sun, J. M.; Xu, Q. H.; Liu, W. M.; Zhang, Z. Q.; Xue, L.; Zhao, P. Palynological evidence for the latest Oligocene-early Miocene paleoelevation estimate in the Lunpola Basin, central Tibet. *Palaeogeogr., Palaeoclimatol., Palaeoecol.* **2014**, *399*, 21−30.
(15) Deng, T.; Wang, S. Q.; Xie, G. P.; Li, Q.; Hou, S. K.; Sun, B. Y. A mammalian fossil from the Dingqing Formation in the Lunpola Basin, northern Tibet, and its relevance to age and paleoaltimetry. *Chin. Sci. Bull.* **2012**, *57*, 261−269.
(16) Fang, X. M.; Dupont-Nivet, G.; Wang, C. S.; Song, C. H.; Meng, Q. Q.; Zhang, W. L.; Nie, J. S.; Zhang, T.; Mao, Z. Q.; Chen, Y. Revised chronology of central Tibet uplift (Lunpola Basin). *Sci. Adv.* **2020**, *6* (50), No. eaba7298.
(17) Xue, W. W.; Najman, Y.; Hu, X. M.; Persano, C.; Stuart, F. M.; Li, W.; Ma, A. L.; Wang, Y. Late Cretaceous to Late Eocene exhumation in the Nima area, central Tibet: Implications for development of low relief topography of the Tibetan Plateau. *Tectonics* **2022**, *41*, No. e2021TC006989.
(18) Leier, A. L.; DeCelles, P. G.; Kapp, P.; Ding, L. The Takena Formation of the Lhasa Terrane, Southern Tibet:The Record of a Late Cretaceous Retroarc Foreland Basin. *Geol. Soc. Am. Bull.* **2007**, *119* (1−2), 31−48.
(19) Zhu, D. C.; Li, S. M.; Cawood, P. A.; Wang, Q.; Zhao, Z. D.; Liu, S. A.; Wang, L. Q. Assembly of the Lhasa and Qiangtang Terranes in Central Tibet by Divergent double Subduction. *Lithos* **2016**, *245*, 7−17.
(20) Zhang, K. J.; Xia, B. D.; Wang, G. M.; Li, Y. T.; Ye, H. F. Early Cretaceous Stratigraphy, depositional Environments, Sandstone Provenance, and Tectonic Setting of Central Tibet, Western China. *Geol. Soc. Am. Bull.* **2004**, *116*, 1202−1222.
(21) DeCelles, P. G.; Kapp, P.; Ding, L.; Gehrels, G. E. Late Cretaceous to middle Tertiary basin evolution in the central Tibetan Plateau: Changing environments in response to tectonic partitioning, aridification, and regional elevation gain. *Geol. Soc. Am. Bull.* **2007**, *119* (5−6), 654−680.
(22) Zhong, L. L.; Zhong, K. H.; Qin, Q.; Yan, Z.; Yang, X.; He, Z. Y.; Zhang, H. J.; Peng, J.; De Grave, J.; Dewaele, S.; Zhou, H. W.; He, X. J.; Han, W. W.; Gong, X. B.; Yang, H. R.; Dong, S. L.; Chang, Y. P.; Li, K. Z.; Dou, J.; Li, L.; He, M. F.; Liu, Y. L. Structural characteristics of the

https://doi.org/10.1021/acsomega.3c09706
ACS Omega 2024, 9, 13148−13162

Nima Basin in the Bangong-Nujiang tectonic belt, central Tibet. *Earth Sci. Front.* **2022**, *29* (1), 266−284. (In Chinese with abstract)
(23) Gongzheng *Research on Sedimentary Facies of Paleogene Source Rocks in Nima Basin, Tibet*; CDUT, 2017 (In Chinese with abstract).
(24) Kong, X.; Mi, W.; Zhu, L.; Yang, W. Zircon U-Pb chronology and prevention of the Paleogene sandstones in the Nima basin, Tibet: implication for copper paleogeography. *Arab J. Geosci* **2019**, *12*, 692.
(25) Gehrels, G. Detrital Zircon U-Pb Geochronology Applied to Tectonics. *Annu. Rev. Earth Planet. Sci.* **2014**, *42*, 127−149.
(26) Chaoqun, Y. *Thermochronology of the Jianghan Basin and peripheral aeras and its implications for the formation of the Yangtze Three Gorges*; CUG, 2022 (In Chinese with abstract).
(27) Wang, T. T.; Ramezani, J.; Yang, C.; Yang, J. H.; Wu, Q.; Zhang, Z. H.; Lv, D. W.; Wang, C. S. High-resolution geochronology of sedimentary strata by U-Pb CA-ID-TIMS zircon geochronology: A review. *Earth-Sci. Rev.* **2023**, *245*, 104550.
(28) Andersen, T. Correction of common lead in U-Pb analyses that do not report ^{204}Pb. *Chem. Geol.* **2002**, *192* (1−2), 59−79.
(29) Vermeesch, P. IsoplotR: A free and open toolbox for geochronology. *Geosci. Front.* **2018**, *9*, 1479−1493.
(30) Zhu, D. C.; Wang, Q.; Cawood, P. A.; Zhao, Z.; Mo, X. X. Raising the Gangdese Mountains in Southern Tibet. *J. Geophys. Res.: Solid Earth* **2017**, *122* (1), 214−223.
(31) Farner, M. J.; Lee, C. T. A. Effects of crustal thickness on magmatic differentiation in subduction zone volcanism: A global study. *Earth Planet. Sci. Lett.* **2017**, *470*, 96−107.
(32) Tang, M.; Ji, W. Q.; Chu, X.; Wu, A. B.; Chen, C. Reconstructing crustal thickness evolution from europium anomalies in detrital zircons. *Geology* **2021**, *49* (1), 76−80.
(33) Huang, X.; Xu, X.; Gao, R.; Guo, X.; Li, W. Shortening of lower crust beneath the netibetan plateau. *J. Asian Earth Sci.* **2020**, *198*, 104313.
(34) Yu, X. J.; Guo, Z. J. Surface uplift of the Tibetan Plateau: Constraints from isostatic effects of Cenozoic sedimentary accumulation. *J. Asian Earth Sci.* **2021**, *208*, 104662.
(35) Corfu, F.; Hanchar, J. M.; Hoskin, P. W. O.; Kinny, P. Atlas of Zircon Textures. *Rev. Mineral. Geochem.* **2003**, *53* (1), 469−500.
(36) Liu, X. H.; Gao, R.; Guo, X. Y.; Ding, L. Detrital zircon U-Pb geochronology of the Lunpola basin strata constrains the Cenozoic tectonic evolution of central Tibet. *Gondwana Res.* **2023**, *113*, 179−193.
(37) Lee, C.-T.-A.; Thurner, S.; Paterson, S.; Cao, W. R. The rise and fall of continental arcs: Interplays between magmatism, uplift, weathering, and climate. *Earth Planet. Sci. Lett.* **2015**, *425*, 105−119.
(38) Li, Y. L.; Wu, X. H.; Zhu, Y. H.; Wang, R.; Zhang, S.; Pang, S. J.; Xiao, R. New display of oil and gas from well Zangshuangdi 1 in Nima basin, Tibet. *Geol. China* **2021**, *48* (6), 1982−1983. (In Chinese)
(39) Yin, S. T.; Zhang, Z. F.; Huang, Y. J.; Zhu, Y. H.; Zhang, S.; Han, Z. P.; Li, Y. L.; Li, X.; Zhao, Y. H.; Liu, J. W. The chemo-stratigraphic analysis for the Paleocene-Eocene Niubao Formation on the section in southern Xiede village, the Nyima Basin, Xizang (Tibet). *Geol. Rev.* **2021**, *67* (3), 667−681. (In Chinese with abstract)
(40) Chen, Y.; Yi, H. S.; Chen, L. J.; Wu, X. H.; Tang, W. Q.; Wang, R.; Yang, Y.; Zhang, C. Z. Astronomical cycles analysis and paleolake level evolution characteristics of Paleogene upper Niubao Formation: A case study of the Ni-1 well in Tibetan Plateau. *Sediment. Geol. Tethyan Geol.* **2023**, *43* (03), 555−564. (In Chinese with abstract)
(41) Mo, X. X.; Zhao, Z. D.; Deng, J. F.; Dong, G. C.; Zhou, S.; Guo, T. Y.; Zhang, S. Q.; Wang, L. F. Response of volcanism to The India-Asia Collision. *Earth Sci. Front.* **2003**, *10* (03), 135−148. (In Chinese with abstract)
(42) Hou, Z. Q.; Mo, X. X.; Gao, Y. F.; Yang, Z. M.; Dong, G. C.; Ding, L. Early Processes and Tectonic Model for the Indian-Asian Continental Collision: Evidence from the Cenozoic Gangdese Igneous Rocks in Tibet. *Acta Geol. Sin.* **2006**, *80* (09), 1233−1248. (In Chinese with abstract)
(43) Zeng, Y. C.; Xu, J. F.; Huang, F.; Li, M. J.; Chen, Q. Generation of the 105−100 Ma Dagze volcanic rocks in the north Lhasa Terrane by lower crustal melting at different temperature and depth: Implications for tectonic transition. *Geol. Soc. Am. Bull.* **2020**, *132* (5−6), 1257−1272.
(44) Geng, Q. R.; Pan, G. T.; Wang, L. Q.; Zhu, D. C.; Liao, Z. L. Isotopic geochronology of the volcanic rocks from the Yeba Formation in the Gangdise zone, Xizang. *Sediment. Geol. Tethyan Geol.* **2006**, *26* (01), 1−7. (In Chinese with abstract)
(45) Xu, Q.; Zeng, L. S.; Gao, J. H.; Zhao, L. H.; Wang, Y. F.; Hu, Z. P. Geochemical characteristics and genesis of the Songka Late Cretaceous adakitic high-Mg diorite in the southern margin of Gangdese, southern Tibet. *Acta Petrol. Sin.* **2019**, *35* (2), 455−471. (In Chinese with abstract)
(46) Shi, H. Z.; Duan, Z. M.; Li, G. M.; Zhang, L. K. Geochemistry and Genesis of the Late Cretaceous Granodiorite in Nulin, Tibet. *Sediment. Geol. Tethyan Geol.* **2020**, *40* (04), 71−82. (In Chinese with abstract)
(47) Hou, D. H.; Pan, Z. L.; Yang, X. P.; Zhang, G. L.; He, J. Y.; Zhang, H.; Cheng, Z.; Wang, S.; Wang, J. G. Chronology, geochemistry and tectonic significance of middle stage of Late Cretaceous adakite in Zhazuo aera, Tibet. *Sediment. Geol. Tethyan Geol.* **2023**, *43* (3), 592−603. (In Chinese with abstract)
(48) Chen, Y.; Zhu, D. C.; Zhao, Z. D.; Meng, F. Y.; Wang, Q.; Santosh, M.; Wang, L. Q.; Dong, G. C.; Mo, X. X. Slab break off triggered ca.113 Ma magmatism around Xainza area of the Lhasa Terrane, Tibet. *Precambrian Res.* **2014**, *26* (2), 449−463.
(49) Wu, H.; Li, C.; Xu, M. J.; Li, X. K. Early Cretaceous adakitic magmatism in the Dachagou area, northern Lhasa terrane, Tibet: Implications for slab roll-back and subsequent slab break-off of the lithosphere of the Bangong-Nujiang Ocean. *J. Asian Earth Sci.* **2015**, *97*, 51−66.
(50) Zhu, D. C.; Mo, X. X.; Zhao, Z. D.; Niu, Y. L.; Pan, G. T.; Wang, L. Q.; Liao, Z. L. Permian and Early Cretaceous tectonomagmatism in southern Tibet and Tethyan evolution:New perspective. *Earth Sci. Front.* **2009**, *16* (02), 1−20. (In Chinese with abstract)
(51) Liu, D. L.; Shi, R. D.; Ding, L.; Huang, Q. S.; Zhang, X. R.; Yue, Y. H.; Zhang, L. Y. Zircon U-Pb age and Hf isotopic compositions of Mesozoic granitoids in southern Qiangtang,Tibet:Implications for the subduction of the Bangong-Nujiang Tethyan Ocean. *Gondwana Res.* **2017**, *41*, 157−172.
(52) Li, J. X.; Qin, K. Z.; Li, G. M.; Xiao, B.; Zhao, J. X.; Chen, L. Magmatic hydrothermal evolution of the Cretaceous Duolong gold-rich porphyry copper deposit in the Bangongco metallogenic belt, Tibet: Evidence from U-Pb and 40Ar/39Ar geochronology. *J. Asian Earth Sci.* **2011**, *41* (6), 525−536.
(53) Gehrels, G. Detrital zircon U-Pb geochronology: Current methods and new opportunities. In *Tectonics of Sedimentary Basins: Recent Advances*; Wiley Online Library, 2011, pp 45−62.
(54) Xue, W. W.; Hu, X. M.; Garzanti, E.; Ma, A.; Lai, W.; Li, C. Discriminating Qiangtang, Lhasa, and Himalayan sediment sources in the Tibetan Plateau by detrital-zircon U-Pb age and Hf isotope facies. *Earth-Sci. Rev.* **2023**, *236*, 104271.
(55) Zhu, D. C.; Zhao, Z. D.; Niu, Y. L.; Mo, X. X.; Chung, S. L.; Hou, Z. Q.; Wang, L. Q.; Wu, F. Y. The Lhasa Terrane: Record of a microcontinent and its histories of drift and growth. *Earth Planet. Sci. Lett.* **2011**, *301*, 241−255.
(56) Pullen, A.; Kapp, P.; Gehrels, G. E.; Vervoort, J. D.; Ding, L. Triassic continental subduction in central Tibet and Mediterranean-style closure of the Paleo-Tethys Ocean. *Geology* **2008**, *36* (5), 351−354.
(57) Dong, C. Y.; Li, C.; Wan, Y. S.; Wang, W.; Wu, Y. W.; Xie, H. Q.; Liu, D. Y. Detrital zircon age model of Ordovician Wenquan quartzite south of Lungmuco-Shuanghu suture in the Qiangtang area, Tibet: Constraint on tectonic affinity and source regions. *Sci. China Earth Sci.* **2011**, *54* (7), 1034−1042.
(58) Leier, A. L.; Kapp, P.; Gehrels, G. E.; DeCelles, P. G. Detrital zircon geochronology of Carboniferous-Cretaceous strata in the Lhasa terrane, Southern Tibet. *Basin Res.* **2007**, *19* (3), 361−378.
(59) Leier, A. L.; Decelles, P. G.; Kapp, P.; Gehrels, G. E. Lower cretaceous strata in the Lhasa Terrane, Tibet, with implications for understanding the early tectonic history of the Tibetan plateau. *J. Sediment. Res.* **2007**, *77*, 809−825.

https://doi.org/10.1021/acsomega.3c09706
ACS Omega 2024, 9, 13148−13162

(60) Kapp, P.; Yin, A.; Harrison, T. M.; Ding, L. Cretaceous-Tertiary shortening, basin development, and volcanism in central Tibet. *Geol. Soc. Am. Bull.* **2005**, *117*, 865−878.
(61) Mi, W. T.; Zhu, L. D.; Yang, W. G.; Yang, L.; Huang, H. Provenance of the Niubao Formation and Its Geological Implications in the North Depression of the Nima Basin in the Tibet. *Earth Sci.* **2017**, *42* (2), 240−257.
(62) Chen, M.; Niu, F. L.; Tromp, J.; Lenardic, A.; Lee, C. T. A.; Cao, W. R.; Ribeiro, J. Lithospheric foundering and underthrusting imaged beneath Tibet. *Nat. Commun.* **2017**, *8*, 15659.
(63) Molnar, P.; England, P.; Martinod, J. Mantle dynamics, uplift of the Tibetan Plateau, and the Indian monsoon. *Rev. Geophys.* **1993**, *31*, 357−396.
(64) England, P.; Houseman, G. Extension during continental convergence, with applicationto the Tibetan Plateau. *J. Geophys. Res.* **1989**, *94*, 17561−17579.
(65) Yin, A.; Harrison, T. M. Geologic evolution of the Himalayan-Tibetan orogen. *Annu. Rev. Earth Planet. Sci.* **2000**, *28*, 211−280.
(66) Chen, J. L.; Yin, A.; Xu, J. F.; Dong, Y. H.; Kang, Z. Q. Late Cenozoic magmatic inflation, crustal thickening, and & > 2 km of surface uplift in central Tibet. *Geology* **2018**, *46*, 19−22.
(67) Ding, L.; Kapp, P.; Yue, Y. H.; Lai, Q. Z. Postcollisional calc-alkaline lavas and xenoliths from the southern Qiangtang terrane, central Tibet. *Earth Planet. Sci. Lett.* **2007**, *254*, 28−38.
(68) Meng, J.; Coe, R. S.; Wang, C. S.; Gilder, S. A.; Zhao, X. X.; Liu, H.; Li, Y. L.; Ma, P. F.; Shi, K.; Li, S. Reduced convergence within the Tibetan Plateau by 26 Ma? *Geophys. Res. Lett.* **2017**, *44*, 6624−6632.
(69) Li, C.; Zhao, Z. B.; Lu, H. J.; Li, H. B. Late Mesozoic-Cenozoic multistage exhumation of the central Bangong-Nujiang Suture, Central Tibet. *Tectonophysics* **2022**, *827*, 229268.

https://doi.org/10.1021/acsomega.3c09706
ACS Omega 2024, 9, 13148−13162